Title

Hydrogen Evolution on Restructured B-Rich WB: Metastable Surface States and Isolated Active Sites

Journal

ACS Catalysis, 10(23)

ISSN

2155-5435

Authors

Zhang, Zisheng
Cui, Zhi-Hao
Jimenez-Izal, Elisa
et al.

Publication Date

2020-12-04

DOI

10.1021/acscatal.0c03410

Peer reviewed

Hydrogen Evolution on Restructured B-rich WB: Metastable Surface States and Isolated Active Sites

Zisheng Zhang,[1] Zhihao Cui,[1,‡] Elisa Jimenez-Izal,[4,5] Philippe Sautet,[1,2,3] Anastassia N. Alexandrova[1,2,]*

[1]Department of Chemistry and Biochemistry, [2]Department of Chemical and Biomolecular Engineering, and 3California NanoSystems Institute, University of California, Los Angeles, Los Angeles, CA 90095

[4]Kimika Fakultatea, Euskal Herriko Unibertsitatea (UPV/EHU), and Donostia International Physics Center (DIPC), P. K. 1072, 20080 Donostia, Euskadi, Spain

[5]IKERBASQUE, Basque Foundation for Science, Bilbao, Euskadi, Spain

KEYWORDS Hydrogen evolution reaction, tungsten boride, surface restructuring, adsorption configuration

ABSTRACT

Borides have been recently identified to be a class of earth-abundant and low-cost materials that are surprisingly active towards oxidative dehydrogenation, and hydrogen evolution reaction (HER) catalysis. Here we explain from first principle calculations the HER activity of WB, an industrial material known for its superior physical properties and chemical inertness. We find that, compared to bulk termination, a major surface reconstruction takes place, leading to the off-stoichiometric B-rich surface termination that contains the active sites. The hydrogen adsorbate configurations are further investigated under various adsorbate coverages. Many competing configurations appear to be accessible in reaction conditions, and thus, a grand canonical ensemble is established to describe the catalytic system. A phase diagram of adsorbate coverages is constructed as a function of pH and applied potential. A complex reaction network is presented based on the ensemble-averaged reaction rates, and the electrocatalytic activities are evaluated under different overpotentials. The major contributors to the activity are found to be a few metastable surface states with distinct electronic structure that are only accessible at high adsorbate coverages in reaction conditions. In addition, while the activity of the dominant active site is nearly the same as on the unreconstructed WB, the B-rich formations play an important role of isolating the active sites, and preventing the passivation of the surface with bubble of forming H_2.

INTRODUCTION

The development of inexpensive and noble-metal-free catalysts for energy and environmental applications is increasingly desirable. Transition metal compounds have recently emerged as a family of promising low-cost electrocatalysts with earth-abundant compositions and satisfying activities, including the transition metal phosphides, sulfides, carbides, selenides, and borides.[1,2] Among the large family of compounds, borides have been the less studied while perhaps the most intriguing, due to the rich chemistry of boron (both covalent, and delocalized and nondirectional bonds, structural diversity).[3–5] A group of transition metal borides, including those of cobalt,[6] nickel,[7] molybdenum,[8] vanadium,[9] and tungsten,[10] has been identified as active electrocatalysts for hydrogen evolution reaction (HER) with a high current density and long-term stability.

Tungsten borides have earth-abundant compositions, and are known for their mechanical hardness, and thermal/electrical properties.[11,12] Tungsten borides with varying stoichiometries, including W_2B, W_2B_5 and WB_4, have been synthesized by solid reaction between tungsten and amorphous boron powders.[13,14] Among these tungsten borides, WB was found to exist in a single crystalline phase, and the crystallinity was found to be enhanced with increasing both time and temperature of heat treatment.[14] WB crystallizes in either an orthorhombic high-temperature phase or a tetragonal low-temperature phase. The latter is stable up to 2,170 ºC, when the phase transition occurs. The low-temperature tetragonal phase is an ultra-incompressible material[15] with a bulk modulus of 428-452 GPa,[16,17] and characterized as superconducting below 4.3 K.[18] This phase is composed of boron chains that alternate to form perpendicular arrays. Thanks to the outstanding mechanical and physical properties of WB, together with its chemical inertness, WB has been widely applied in industry for cutting tools and coatings. Thus, it came as a surprise that tungsten borides should be so active towards electrocatalytic HER.

Recent findings point out the likely common structural feature of boride surfaces: the presence of the excess boron. Firstly, it is generally known that the boride synthesis requires large off-stoichiometric excess of boron. Borides of many transition metals and also hexagonal boron nitride show analogous selectivities toward propane oxidative dehydrogenation (ODH),[19,20] which was attributed to the partially oxidized amorphous boron layer that forms on their surfaces *in situ* in oxidizing conditions, and restructures in timescale of picoseconds.[21,22] Additionally, we found that boron-rich structures and monolayers can form on the tungsten metal, with the restructuring unlocking novel electronic properties of the boron.[23] Encouraged by these works, we combine global optimization techniques and density functional theory (DFT) to explore the structural diversity of the WB (001) surface with different coverage of excess boron. By calculating the surface energies of the bare WB surfaces with different terminations and the B-excess surfaces with different stoichiometries as functions of the chemical potential of boron, we estimate their relative stabilities, and propose a B-rich WB surface as the actual present phase. In order to assess the activity for HER, the configurations for H adsorbates on this B-rich surface under different H coverages are then explored, to construct a grand canonical ensemble where the population of each surface state changes as a function of chemical potential of H. By including potential-dependent and pH-dependent terms into the chemical potential of H, the population of each surface state and the ensemble-averaged reactivity can be evaluated under various reaction electrocatalytic conditions. We demonstrate that it is crucial to account for surface restructuring and multiple accessible adsorption configurations under a grand canonical scheme to properly describe the catalytic interface under realistic conditions.

RESULTS AND DISCUSSION

In order to determine the most stable surface terminations of WB, we explored all the possible low-index surfaces with different terminations and calculated their surface energies. Specifically, we characterized the (100), (110), (201), (210), and (310) surfaces, as well as the (001), (101), and (111) surfaces with both B and W terminations, and the results are summarized in Table S1. It can be seen that the B-terminated surfaces are generally more stable. This scenario is similar to oxide surfaces, where the more electronegative oxygen is more likely to be exposed, though electronegativities of W and B are much closer than those of metals and O. Note that several terminations, such as B-(001) (γ= 3.59 J/m^2) and (111) (γ= 3.23 J/m^2) , have similar surface energies to that of other superhard materials, such as diamond (γ= 3.76 J/m^2) and ReB_2 (γ= 3.00 J/m^2).[24,25] Judging from the calculated surface energies, only the B-terminated (111) and (001) surfaces will be exposed, while the contribution from other surface terminations would be minor and can be neglected.

Because of the large unit cell of the (111) facet and the exponentially growing computational cost of global optimization with increasing cell size, we focused on the (001) facet and thoroughly explored its different non-stoichiometric terminations. A conclusion that will eventually emerge in this study, is that similar structural and electronic effects responsible for catalysis are expected to occur on other terminations as well. First, the (001) surface can be cut using four different terminations, including two stoichiometric structures (W terminated W-(001) and B terminated B-(001) surfaces), and two non-stoichiometric ones (W-rich and B-rich (001)). Second, in addition to these ideal cuts, we explored a wider variety of possible terminations using the particle swarm optimization (PSO) algorithm combined with density functional theory (DFT) calculation by varying the number of surface B atoms per unit cell from 0 to a maximum of 8.

The surface energy of the global minimum termination of each composition under varying chemical potential of B (μ_B) is shown in **Figure 1** (lower surface energy corresponds to higher stability). At the lower limit of μ_B, the B terminated stoichiometric surface is more stable than the B-rich ones. As the values of μ_B increases, the thermodynamically most stable state shifts from the stoichiometric terminations to the B-rich terminations. Because experimentally transition metal borides are synthesized by reacting metal with elemental boron in the powder form, the μ_B in synthetic condition should be that of elemental boron. Therefore, the region around the μ_B of elemental boron would be the most chemically relevant to the realistic termination of WB surface (highlighted region in **Figure 1**), and the actual (100) surface structure present in WB is hence predicted to be the B-rich surface with hexagonal island-like B_8 clusters. Note that the shape and size of the cluster may change if a larger unit cell would be used in global optimization. However, a likely general qualitative conclusion can be made that the boron forms islands on the surface, and some nearly isolated W atoms or rows of W atoms remain exposed at the relevant μ_B.

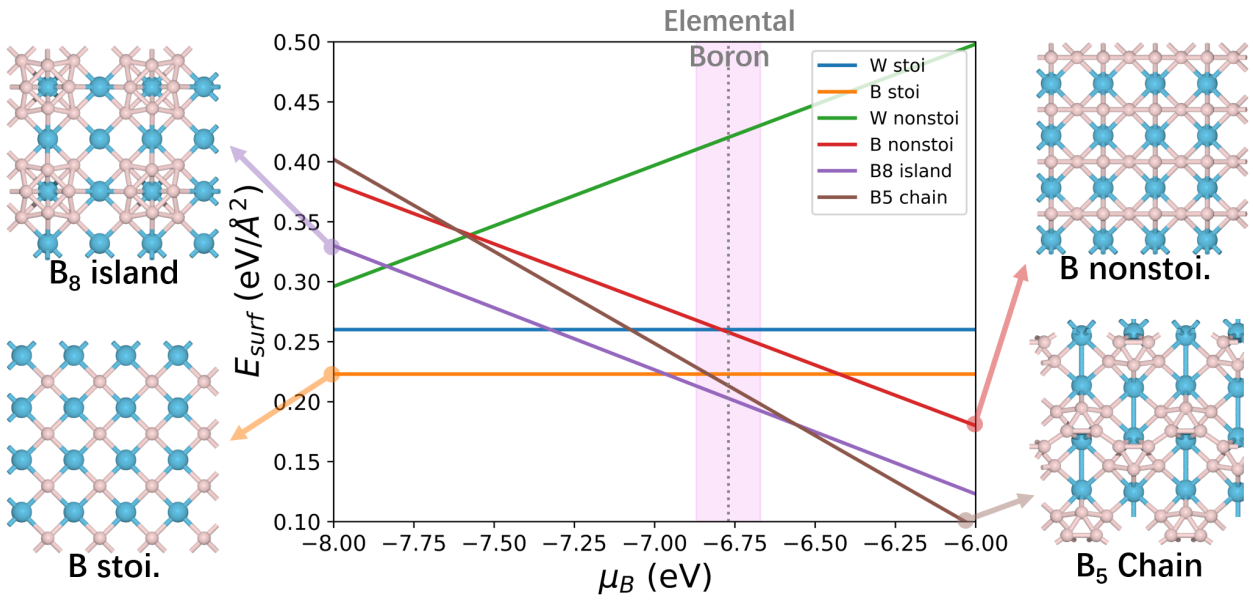

Figure 1. Surface energy of W stoichiometric, B stoichiometric, W nonstoichiometric, B nonstoichiometric, B_8 island, and B_5 chain terminations under different μ_B, with optimized geometries of the surfaces of interest shown on left and right side of the plot. The μ_B of elemental boron is marked by dotted line, and the region around it is highlighted with violet shade. Color code: B (pink), W (blue).

The binding energies of typical adsorbates that are common in heterogeneous catalysis and electrocatalysis on the bare WB (001) and B_8-decorated WB (001) are calculated and summarized in **Table S2**. The presence of the B_8 island not only alters the adsorption values on original sites but also introduces new binding sites. The binding energy of H on the B_8 island is comparable to that of Pt, which, although is a crude estimation, motivated us to further investigate the surface chemistry of the B_8-decorated WB (001) under the HER conditions. The restructured surface has a more complex structure compared to the original WB surface; hence, it is expected to provide multiple kinds of new H adsorption sites. To explore all the chemically relevant adsorbate

configurations on the B_8-decorated surface, we exhaustively sampled the adsorbate configurations with the coverage of 1-8 H atoms per unit cell to obtain all the accessible minima. **Figure S1** and **Table S3** summarizes the energies and geometries of the found surface states. The surface structures are referred to as *m*H#*n*, where the *m* is the coverage of adsorbates (number of H's per unit cell) while *n* means it is the *n*-th minimum (#1 stands for global minimum) within the *m*H coverage. Note that the upper limit of 8 H per unit cell is chosen because the 8H surface cannot uptake any more H without disintegration of the B_8 unit, and such configurations are energetically unstable.

We find that there are several low-energy minima (within 0.5 eV from GM) at each coverage at room temperature, and there are essentially four distinct adsorption sites: top-layer B, sub-layer B, type-1 W, and type-2 W (Fig. 2 a) Top-layer B is the feature site of the B_8-island surface; each such B is forming a 4-member ring with the other 3 top-layer B atoms while also bonded to two buried W atoms and two sub-layer B atoms. Note that the top-layer B contains two kinds of sites that differ in underlying atoms (B or W), but their energetics show minor difference (~0.1 eV) and has similar trend as coverage increases, so we merge them in this classification. These sub-layer B atoms are in a similar location as the surface B in the stoichiometric surface. Such unit can host a H adsorbate in a bridging manner under higher coverages. Type-1 W is the surface W site that is more exposed, i.e. not being covered by or directly bonded to the top-layer B atoms. It can bind H in a similar atop position as the surface W in the stoichiometric surface does (**Figure S2**), and it can bind up to two H atoms under higher coverage. Type-2 W atoms are less exposed compared to type-1 W atoms, and the H adsorbate on it tends to bridge between the type-2 W and the neighboring top-layer B. Each type of site is labeled on the structural model in **Figure 2a**.

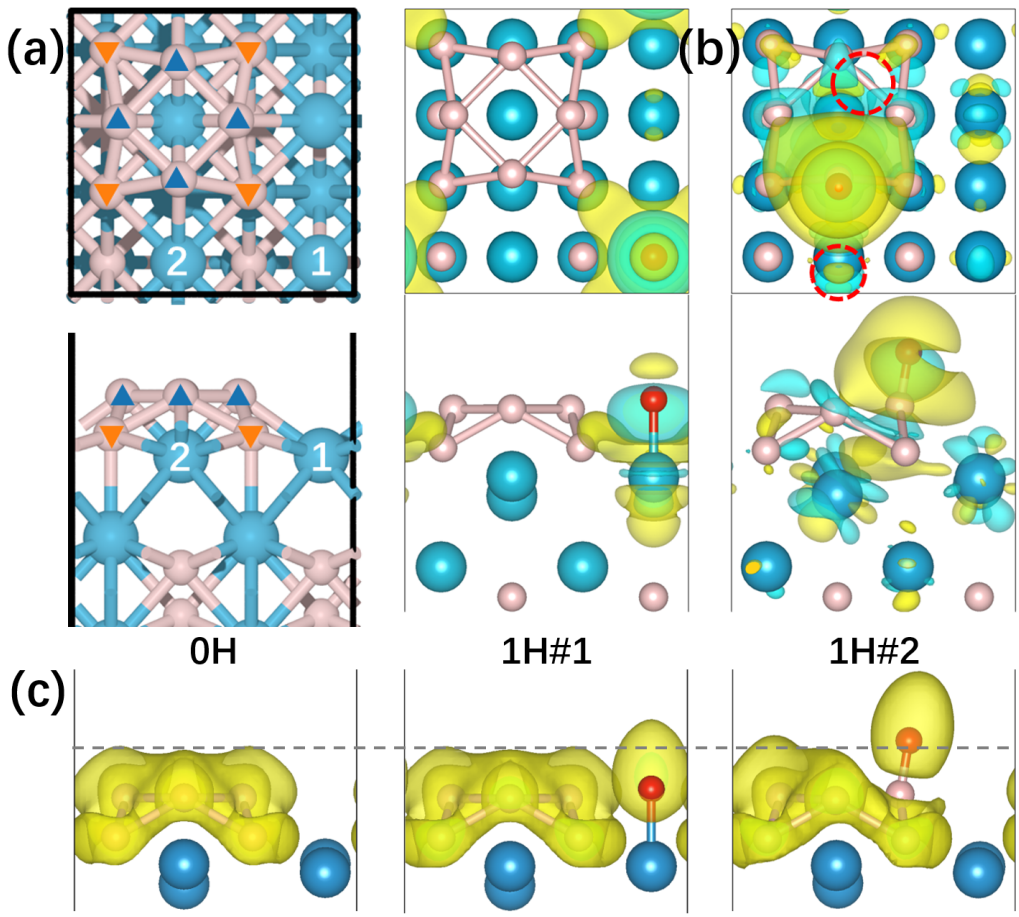

Figure 2. (a) Optimized geometry of the WB (001)-B_8 island structure from top and side view, with top layer B, sub layer B, type-1, and type-2 W atoms marked with blue triangle, orange inverted triangle, number "1" and "2", respectively. (b) The electron density difference map of H adsorption on W or B sites of B_8-decorated surface at isovalue=0.0015, with blue and yellow isosurfaces representing increase and decrease in electron density, respectively. (c) The electron localization function plot of 0H, 1H#1, and 1H#2 surface states at isovalue=0.475. Color code: H (red), B (pink), W (blue).

At the 1H coverage, the global minimum (GM) structure 1H#1 has H adsorbed on type-1 W, which is consistent with the stoichiometric surface case where H is also on W in the GM structure. When the H coverage is increased, surprisingly, the type-1 W is no longer the preferred adsorption site. In 2H#1, 3H#1, and 4H#1, all H atoms are adsorbed on top-layer B, while the configurations with H on type-1 W are the less stable second or the third local minima. Not until the coverage reaches 5H does the GM begin to contain again one H on type-1 W.

To investigate the reason for such change in adsorption behavior upon increasing coverage, the electron density difference of H adsorption on top-layer B and type-1 W are calculated. In **Figure 2b**, it can be seen that, upon H adsorption on type-1 W, the electron density over the W and its surrounding sub-layer B's are reduced, while the region around the W-H bond increases. This can be attributed to the electron transfer from the W-B bonding orbitals to the W-H σ orbital. Note that this electron transfer is highly localized, with the electron density of sub-layer B's going through a minor decrease and the top-layer B's being unchanged. In 1H#2, however, a much more significant and delocalized electron transfer can be observed. The electron density over the adsorption site and its neighboring B atoms suffers substantial depletion. From the electron localization function (ELF)[26] plot in **Figure 2c**, we see that the B_8 island is held together by a strong conjugation formed via the overlap of both $\pi -$ and $\sigma -$bonds between them (a known bonding phenomenon for boron clusters).[4] Such conjugation is almost unaffected upon H adsorption on type-1 W, but it is broken when the H goes onto the top-layer B site. The weakening of conjugation system can also be evidenced by lengthening of the B-B bonds as the number of H on top-layer B sites increases from 0H to 4H, as is shown in **Figure 3a**. Surprisingly, upon the weakening of conjugation near the adsorption site, the electron density increased on the other side of the top-layer B sites which are "freed" from the conjugation. As a result, the neighboring top-

layer B sites would be "activated" to bind the next adsorbate stronger, and that explains why the top-layer B sites become more favorable at higher coverage than the W sites. Such change in electronic structure can be evidenced by the increase of electron density in the circled region in **Figure 2b** and the expansion of ELF isosurface beyond the original one (marked by grey line in **Figure 2c**). The emerging electron-rich region between the top-layer B sites on the other side gives rise to the bridging adsorption site over three B atoms in 2H#6. The type-2 W next to the adsorption site is also freed from the conjugation system, and electron density increases on the other side, leading to formation of bridging adsorption site between a type-2 W and a top-layer B. Since the conjugated system is broken as the B_8 island gets hydrogenated, the structural stability of the B_8 island under H coverage could be questioned. Therefore, Born-Oppenheimer molecular dynamics (BOMD) simulation of the 3H#1 surface state, whose B_8 island is partially covered by H, is performed at an elevated temperature of 500 K (**Figure S3**). The structure of partially covered B_8 stays rather stable during the simulation, with the RMSD of all atoms being only c.a. 0.13 Å. The B atoms in the B_8 island and the adsorbed H atoms do move during the simulation, with a relatively large RMSD of c.a. 0.30 Å and c.a. 0.37 Å, respectively, but there is no bond breakage, nor H migration. In conclusion, despite the weakening of conjugated system over the B_8 island, the surface should maintain its structural integrity at room temperature.

To quantitatively study the electron transfer accompanying the adsorption events on B_8 island, we calculate the Bader charge of the atoms in 1H#1, 2H#1, 2H#2, 3H#1, 4H#1, and 5H#1, as summarized in **Figure S4**. The H gains ~0.4 negative charge upon adsorption as a result of electron transfer from the top-layer B in 1H#1, suggesting that a more negative Bader charge on the site would facilitate adsorption. The other B atoms in the B_8 island also gain negative charge of -0.02 ~ -0.12 due to the disruption of the conjugated system, activating them to be more favorable

adsorption sites under higher coverages. The H adsorption on type-1 W, however, does not lead to a so pronounced charge transfer to surrounding atoms. As we increase the H coverage from 1 to 4 and focus on surface states where top-layer B's act as adsorption sites, the sum of Bader charge of top-layer B's keeps increasing, while sub-layer B's gain a share of electrons released from disruption of conjugate system (**Figure 3c**). Overall, the B_8 island loses electrons with increasing H coverage. In **Figure 3b**, it can be seen that the charge transfer to H is mostly contributed by the B_8 island with little participation of the WB substrate, indicating that the restructured layer of excess boron could be generally present on borides and the intrinsic properties of B-rich layer is somewhat substrate-independent. This qualitative conclusion also likely translates to the (111) surface of WB, which we did not investigate here.

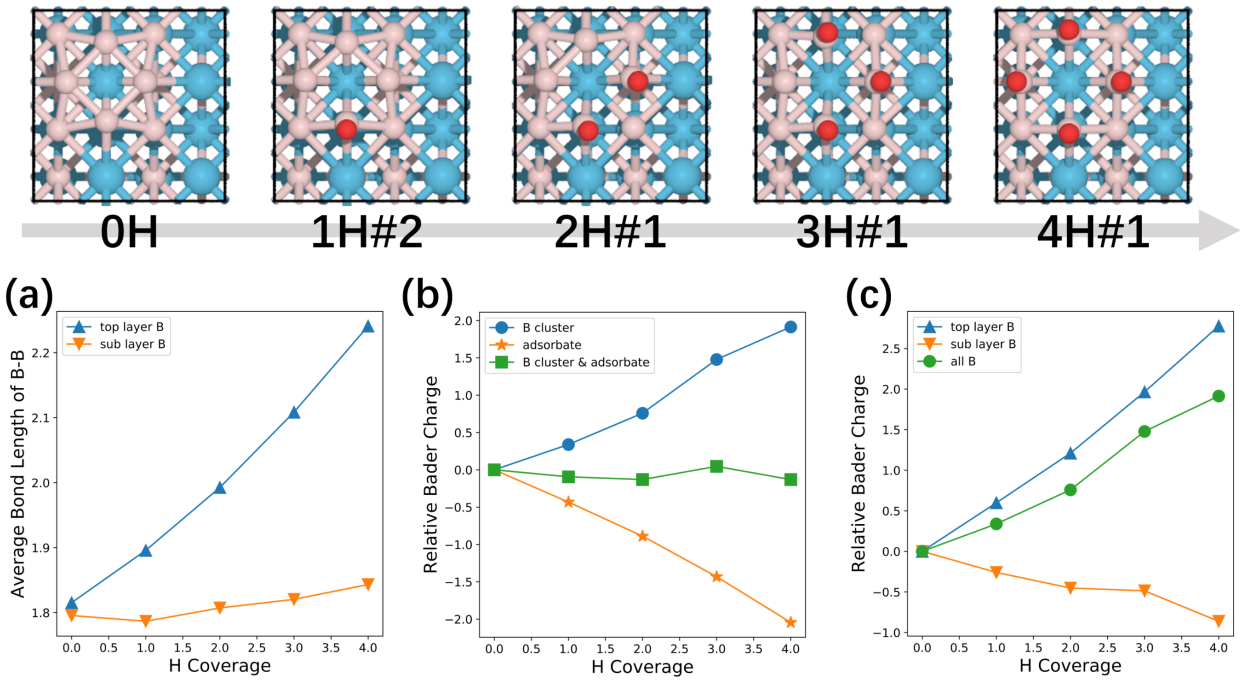

Figure 3. (a) The bond length versus number of H plot of top layer B-B and sub layer B-B, and calculated average Bader charge values of (b) B island, adsorbate and B island with adsorbate and (c) top layer, sub layer and all surface B for featured surface states coverages from 0H to 5H. The

optimized geometries of the selected surface states are shown above the plots. Color code: H (red), B (pink), W (blue).

After understanding the change in electronic structure induced by adsorption of adsorbates, we go back to investigate the HER activity. The hydrogen evolution reaction has two steps:

$$* + \mathrm{H}^+ + \mathrm{e}^- \rightarrow * \mathrm{H} \qquad (1)$$

$$* \mathrm{H} + \mathrm{H}^+ + \mathrm{e}^- \rightarrow * + \mathrm{H}_2 \qquad (2)$$

Where the * and *H stand for the active site and the adsorbed H species on the surface. The chemical potential of H^+ and e^- can be expressed by the chemical potential of hydrogen gas using the computational hydrogen electrode model. Since the activation barrier of the proton-electron transfer has been demonstrated by numerical calculations and theoretical considerations to scale with $\Delta \boldsymbol{G}$,[27–29] the barrier of HER steps can be described by $\Delta \boldsymbol{G}_{\mathrm{H}}$.[30] It comes naturally that the optimal HER active site would have $|\Delta \boldsymbol{G}_{\mathrm{H}}| \approx 0$ because too positive $\Delta \boldsymbol{G}_{\mathrm{H}}$ means difficulty in step (1), while too negative $\Delta \boldsymbol{G}_{\mathrm{H}}$ leads to slow step (2). Note that the possibility of Volmer-Tafel mechanism is also tested, but the energy barrier for dihydrogen formation from two *H is too high (>1.5 eV), and the Volmer-Heyrovsky mechanism prevails. This is probably due to the more directional H binding and less favorable H migration on the B_8 unit as compared to the case on noble metals such as Pt.

In the conventional practice, the most stable structure, or the GM, at each coverage would be used to calculate the $|\Delta G_H|$ which would then serve as the activity descriptor for the HER. However, the structural diversity of our B_8 island surface under different coverage casts doubt on the

conventional practice: although 1H#1 is more stable than 1H#2, it structurally mismatches 2H#1 (**Figure 3**), the most stable surface state under 2H coverage; instead, it is the thermally-accessible 1H#2 and 1H#3 metastable states that can uptake an additional H to become 2H#1. In terms of geometry, only if the * and *H intermediates structurally match will the reaction step make chemical sense. The infeasibility is supported by energetics: going from 1H#2 to 2H#1 only involves a single step H-adsorption, while going from 1H#1 to 2H#1 requires a direct migration of adsorbed H from type-1 W to top-layer B beforehand, which is not only thermodynamically uphill but also has a prohibitively high barrier of 1.67 eV (**Figure S5**). Therefore, some reaction paths with seemingly favorable energetic should be excluded if the geometries of the initial and final species do not match. Hence, we include all the local minima at each coverage into our model, and evaluate the structural similarity of each possible pairs of * and *H. To be specific, we calculated the mean atomic displacement (***D***), for each pair of * and *H:

$$\boldsymbol{D} = \frac{1}{\boldsymbol{N}} \sum_{\boldsymbol{n}=1}^{\boldsymbol{N}} |\boldsymbol{r}_{n,\mathrm{f}} - \boldsymbol{r}_{n,\mathrm{i}}|$$

Here $\boldsymbol{N}$ is the total number of atoms in *, $\boldsymbol{r}_n$ is the position vector of the n-th atom in the structure, i and f stand for the initial and final state, respectively. By eliminating the */*H pairs with mean atomic displacement larger than 0.025 Å, we keep only 88 relevant pairs (listed in **Supplementary Note 1**) out of the 349 pairs and plot them into a circular graph in **Figure 4**. The nodes represent surface states, and they are colored in spectral color map according to H coverage. Each edge connecting a */*H pair represents a unique HER catalytic cycle, interweaving into a complex reaction network.

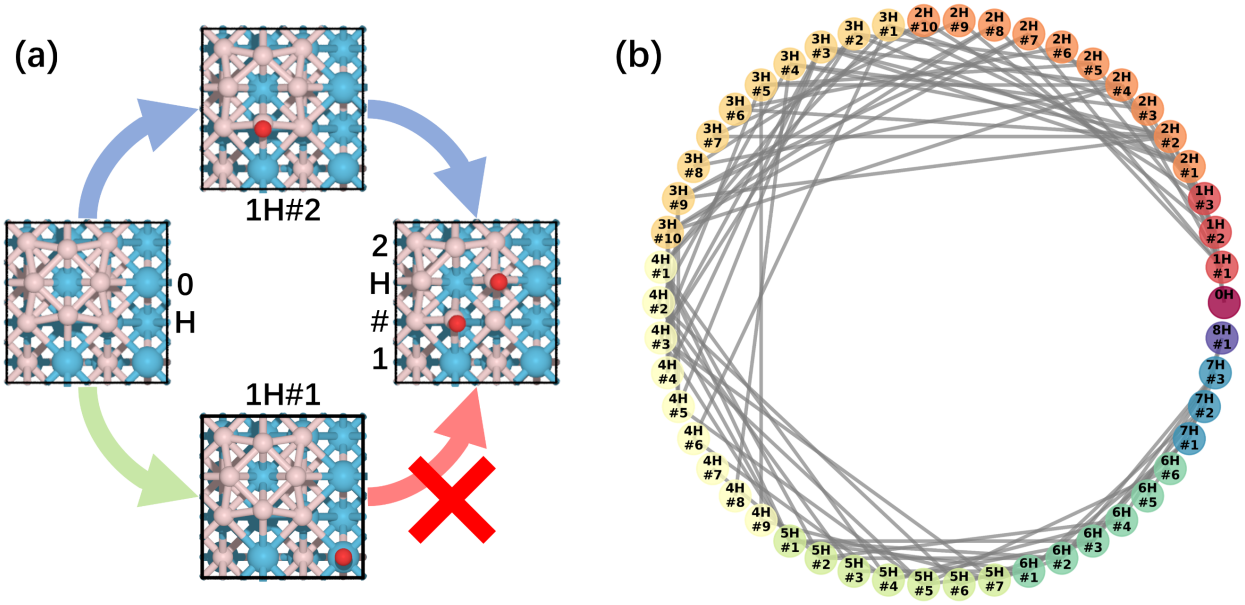

Figure 4. (a) An illustration of accepted and rejected HER reaction paths connecting minima. Color code: H (red), B (pink), W (blue). (b) The full reaction map of all viable reaction pathways based on the found minima in this study. Each node in the graph represents a surface state with its color showing its corresponding adsorbate coverage (warmer: lower coverage; colder: higher coverage). Every connecting line stands for a reaction path with matched geometry between initial and final states.

Figure 5a shows the distribution of $\Delta \boldsymbol{G}_{\mathrm{H}}$ of all the feasible HER pathways in **Figure 4b** with the region near $\Delta \boldsymbol{G}_{\mathrm{H}} = 0$ marked by gray dotted line. It is a rather wide distribution ranging from c.a. -0.9 eV to +0.7 eV, indicating binding sites of diverse electronic structures that result from different adsorbate coverages and configurations. There are some pathways with optimum $\Delta \boldsymbol{G}_{\mathrm{H}}$, however, we may have too few of them in the reaction condition to contribute significantly to the overall activity. Hence, it is crucial to quantitatively calculate the population of each surface state. In a realistic scenario, the surface exists as an ensemble of surface states of different adsorption

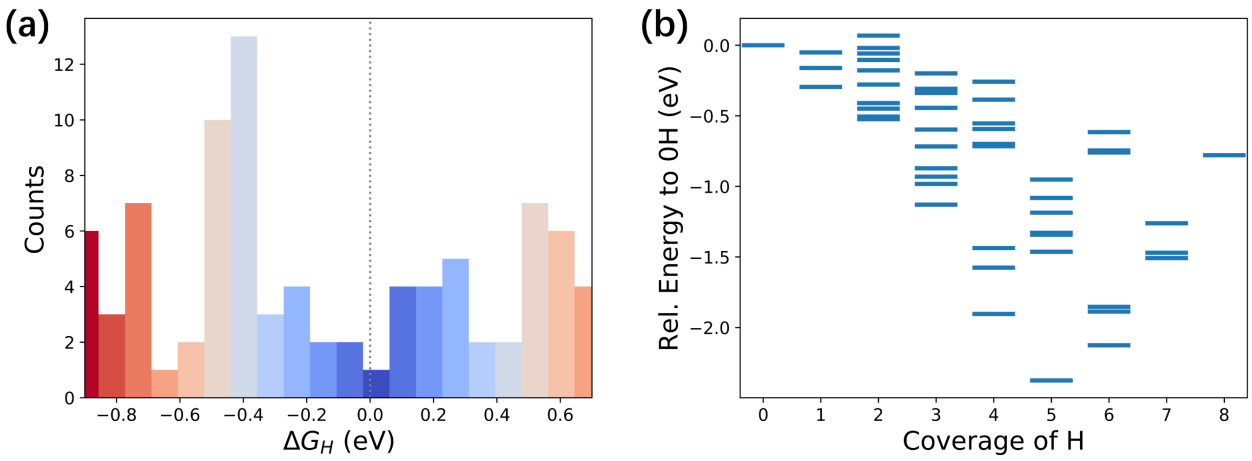

Figure 5. (a) The histogram showing distribution of ΔG_{H} of the feasible HER pathways, with cold and warm color representing favorable and unfavorable HER energetics, respectively. The dashed line marks the optimal $\boldsymbol{\Delta G_{\mathrm{H}}}$ value for HER. (b) The relative free energies of each surface state from different coverages under the grand canonical scheme at $U = 0$ V (vs. SHE) and pH = 0, with the 0H surface state as zero reference.

configurations within each coverage, and every surface state contributes to the overall activity to some extent.[31] To obtain the population of each surface state, a grand canonical ensemble can be established based on the grand canonical free energy Ω:

$$\Omega = A(* n\mathrm{H}) - n\mu_{\mathrm{H}^+}(U, p\mathrm{H}) - n\mu_{\mathrm{e}^-}(U, p\mathrm{H})$$

Where n is the number of adsorbed H atoms, $A(* nH)$ is the free energy of the surface state with n adsorbed H atoms. $\mu_{\mathrm{H}^+}(U, p\mathrm{H})$ and $\mu_{\mathrm{e}^-}(U, p\mathrm{H})$ are the electrochemical potential of proton and electron. Under the CHE scheme, the chemical potential of an electron-proton pair can be approximated in reference to the free energy of half a dihydrogen molecule, and it also allows the effect of applied potential and pH to be facilely included in the model.[32,33] **Figure 5b** shows the free energies of the surface states of different H coverage relative to the 0H case at $U = 0$ V (vs.

SHE) and pH = 0. The 5H#1 has the lowest energy among all surface states and is therefore the most populated state at that specific reaction condition. Since changes in U and pH can reshape the energy landscape by altering the $\boldsymbol{\mu}_{\mathrm{H}}$ term, the global minimum of the grand canonical ensemble can shift at different reaction conditions. Since the aqueous solution can act as a proton reservoir at finite temperature and proton can diffuse through the water-hydronium network without much of a kinetic barrier, we assume the ensemble to be ergodic, i.e. surface states with the same or different coverage can interconvert and reach an equilibrium. Therefore, the population of each surface state can be calculated by the Boltzmann distribution:

$$p_i = \frac{exp\ (-\frac{\Omega_i}{kT})}{\sum_{j=1}^{N} exp\ \left(-\frac{\Omega_j}{kT}\right)}$$

Where in this case T = 298 K. The population of each surface state can then be readily calculated at any given reaction conditions. In **Figure 6a**, the ensemble-averaged H coverage is shown as a function of U and pH in their experimental range. In alkaline media, the B_8 unit remains structurally intact and the surface tends to stay intact in the 0H coverage. When the μ_{H} increases to a threshold by increasing acidity or applying more negative potential, the surface quickly converts to 4H coverage over a very small range of μ_{H}. This can be attributed to the activation of neighboring B sites in the B_8 unit upon the first H adsorption until all four top-layer B atoms are covered which is discussed in previous sections. After that, the 4H surface states accept another H onto the type-1 W site and stay in the 5H coverage over a pretty wide window of μ_{H}. Note that in the realistic scenario of HER in alkaline media, alternative reaction mechanism with different kinetics may come in play, therefore the reactivity evaluation based on the grand canonical ensemble would only hold in the neutral-acidic media. Since the HER is usually performed with

pH ranging from 0 to 7 and U ranging from 0 to -0.5 V vs. SHE, we would expect only the 5H and higher coverages in the working condition.

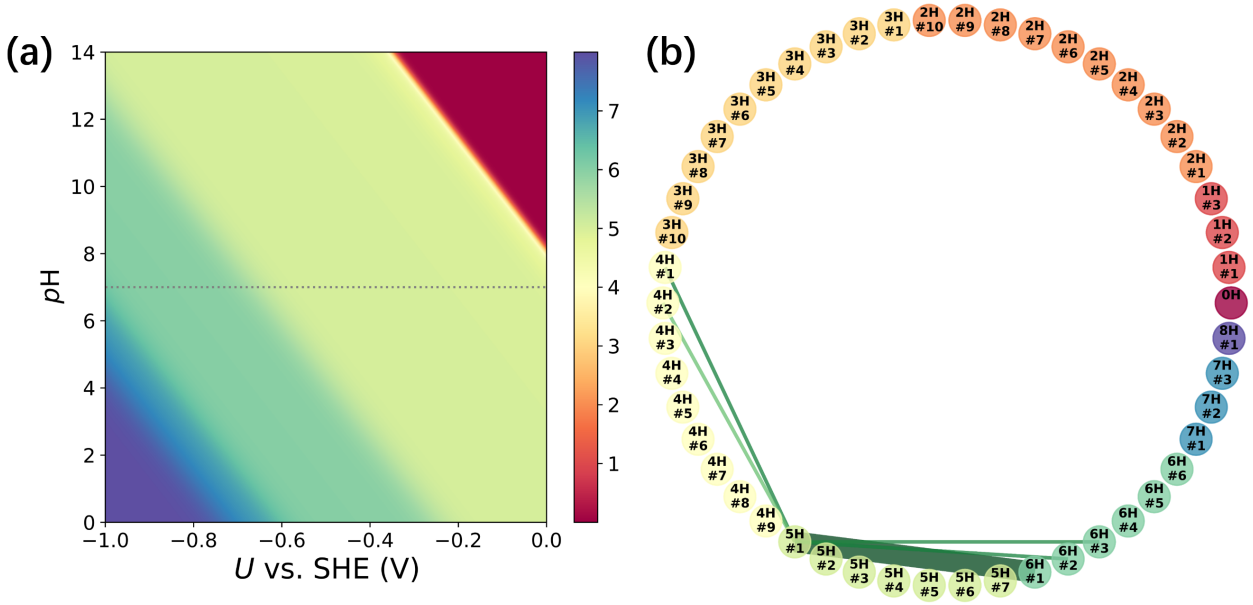

Figure 6. (a) Phase diagram of hydrogen coverage on B_8-decorated surface as a function of pH and applied potential. The grey dotted lines mark the neutral pH condition. (b) A revised reaction map that also shows the activity contribution from each reaction pathway, with the major contributor in thicker line and darker green while minor contributors in thinner line and lighter green.

It is then clear that neither the population, nor $|\Delta G_H|$ can act as a proper descriptor of the HER activity, and both must be included in our model. Since ΔG of an electrochemical step under CHE scheme scales with the electrochemical barrier, the reaction rate of the elementary redox steps (1) and (2) involving any feasible pair of * and *H (denoted as i and j) under constant pH can be expressed by the Arrhenius-type equation as:

$$\text{Step 1: } r_{\mathrm{f},ij} = k_{\mathrm{f},ij}[*] \propto \exp\left(-\frac{\Delta G_{\mathrm{f}}(U)}{kT}\right) \cdot p_i$$

$$\text{Step 2: } r_{\mathrm{r},ij} = k_{\mathrm{r},ij}[* \mathrm{H}] \propto \exp\left(-\frac{\Delta G_{\mathrm{r}}(U)}{kT}\right) \cdot p_j$$

Where the $\Delta G_{\mathrm{f}}(U)$ and $\Delta G_{\mathrm{r}}(U)$ are the potential-dependent free energy change of forward (1) and reverse (2) reaction step, and the p_i and p_j are population of the * and *H sites calculated from Boltzmann distribution in the grand canonical ensemble, respectively. The overall rate r_{ij} of the step concerning surface states *i* and *j* can then be calculated from a Butler-Volmer-type equation:

$$\mathrm{r}_{ij} \propto \exp\left(-\alpha \frac{\Delta G_{\mathrm{f}}(U)}{kT}\right) \cdot p_i - \exp\left(-(1-\alpha)\frac{\Delta G_{\mathrm{r}}(U)}{kT}\right) \cdot p_j$$

Where the $\alpha \in [0,1]$ is the mechanistic symmetry factor. Here we adopt the value of $\alpha = 0.5$ assuming no asymmetry about the equilibrium potential. The net rate $\boldsymbol{r}_{\mathrm{net}}$ of the HER involving *i* and *j* is taken to be the smaller overall rate between those of step (1) and (2), and it could act as a descriptor of the activity contribution from a specific pathway. In **Figure 5b**, we replot the edges representing */*H reaction pairs with color map and thicken the edges with large $\boldsymbol{r}_{\mathrm{ij}}$ (evaluated at pH = 0 and U = 0.1 V vs. SHE). The */*H pairs with the largest HER rates are 5H#1/6H#1, 4H#1/5H#1, 5H#1/6H#2 and 5H#1/6H#3. Although the 5H#1/6H#1 pathway does not have fully optimal $|\Delta G_H|$, the 5H#1 surface state has so dominant population that the 5H#1-related pathways prevail in terms of net HER rate. Some other pathways with near-zero $|\Delta G_H|$, such as 2H#1/3H#3 and 2H#6/3H#6, turn out to show negligible activity since the related surface states are inaccessible. The weighted reaction map presents a vivid illustration that it is the surface states with significant population and decent energetics, instead of the ones with the most optimal $|\Delta G_H|$, that contribute to the overall reactivity.

It is also straightforward to track the effect of varying overpotential on sites contributions to overall HER rate based on this grand canonical ensemble representation. In **Figure 7**, we break down the total HER rates to percentage contributions of the four major pathways at pH = 0. In the potential range of 0 to -0.5 V vs. SHE, the HER is solely contributed by the 5H#1/6H#1 pathway. The 5H#1/6H#1 has a $|\Delta G_H|$ of 0.249 eV, corresponding to an overpotential of 249 mV which is in good agreement with the experimental value on tungsten boride in the U = 0 ~ -0.5 V range (give value).[10] As the potential goes to -0.6 V vs. SHE, the 6H surface states gains population, and 5H loses, so that the 6H#2/7H#1 and 6H#3/7H#2 become the top two contributors to the overall HER activity, which correspond to overpotential of ~380 mV if not limited by population. At more negative potentials, the 8H coverage, also the completely hydrogenated form, gets populated, and the 7H#3/8H#1 becomes the major reaction pathway with an overpotential of 480 mV, if not limited by the population. It is seen that, as the potential gets more negative, the surface is driven into a higher H coverage region where the accessible HER pathways involve low-population metastable sites and have inferior intrinsic reactivity compared to the lower-coverage cases. This suggests a reactivity decline of the boride catalysts at high overpotentials or in too acidic media. Such a trend is similar to the HER on metal surfaces where reactivity of the surface is optimal under intermediate H coverage but worsens near full coverage. Note that many of the surface states involved are accessible local minima of their coverage, and they are necessary for a full and correct depiction of the HER process on B_8-decorated WB (001).

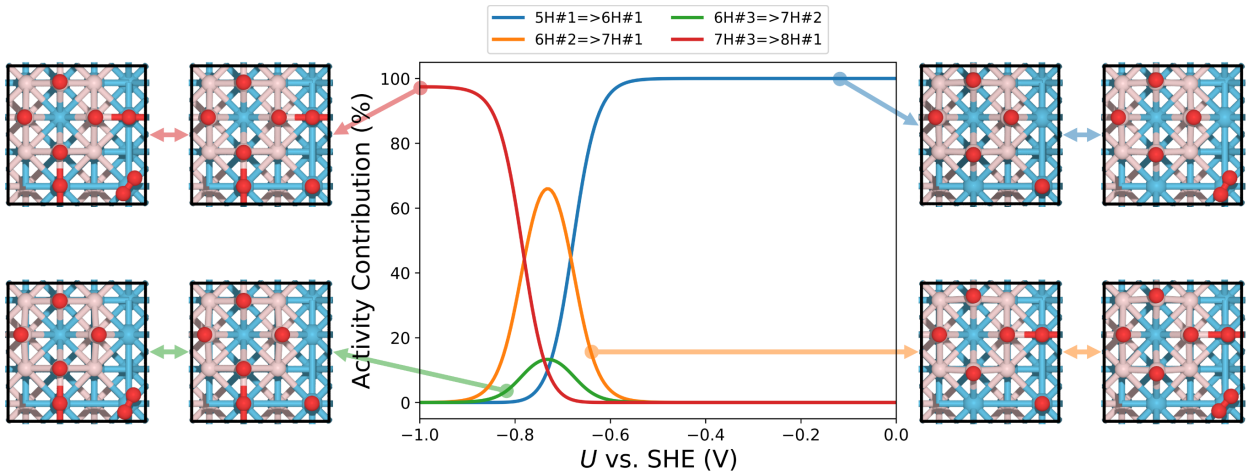

Figure 7. Activity contribution in percentages of the four most active surface states versus the applied potential. The optimized geometries of the involved surface states are shown on the left and right sides of the plot. Color code: H (red), B (pink), W (blue).

It is somewhat surprising that all the major contributing pathways involve the same W-H/W-H_2 cycle on type-1 W site, motivating us to further investigate the role of B_8 island at higher coverage cases. The electron density difference map in **Figure 8a** shows that, upon the formation of B_8 island on the surface, the electron density on the type-2 W is depleted, while the density on the type-1 W increases. In addition, the electron density from B_8 unit spreads out to cover the region over type-2 W sites, destabilizing the W-H configuration, and the formation of W-H_2 on the type-2 W sites. **Figure 8b** shows the bonding nature of W-H_2 unit: a small amount of electron is donated by type-1 W to the region between the two H atoms above (also evidenced by Bader charge in **Figure S4**), forming W-H bonds while also giving rise to a σ-type bond between two H adsorbates. However, the change in electron density over type-1 W induced by formation of B_8 is actually minor, and the energetics of the W-H/W-H_2 cycle is similar on the B_8-decorated and the bare WB

(001). The major role of B_8 is that it suppresses the H adsorption on type-2 W sites next to the active type-1 W site, and ensures that the surface state with W-H_2 unit has a significant population at higher H coverages. Such suppression is absent on the stoichiometric WB (001) surface where the second H adsorbate tends to reside on the neighboring W site instead of forming a favorable W-H_2 species (**Figure S2**). In addition, the physisorption of H_2 on the B_8 unit is unfavorable (**Figure 8c**), and such effect extends to the region over the type-2 W sites, effectively isolating the active type-1 W atoms from each other in a single-site fashion. This should have an unusual and important effect on the HER activity of the B-rich surface: The formed H_2 will not accumulate as large flat gas bubbles that cover the surface of catalysts and passivate it. The bubble effect is a common problem in HER on catalysts where active sites are densely distributed, such as metals, phosphides, and chalcogenides.[34] The B_8 islands that formed from restructuring of excess boron could effectively act as sub-nano aerophobic units and prevent the gas accumulation problem. This could also explain the outstanding stability of the borides in long-term and high-current-density electrocatalysis without elaborate nanostructuring.[10]

20

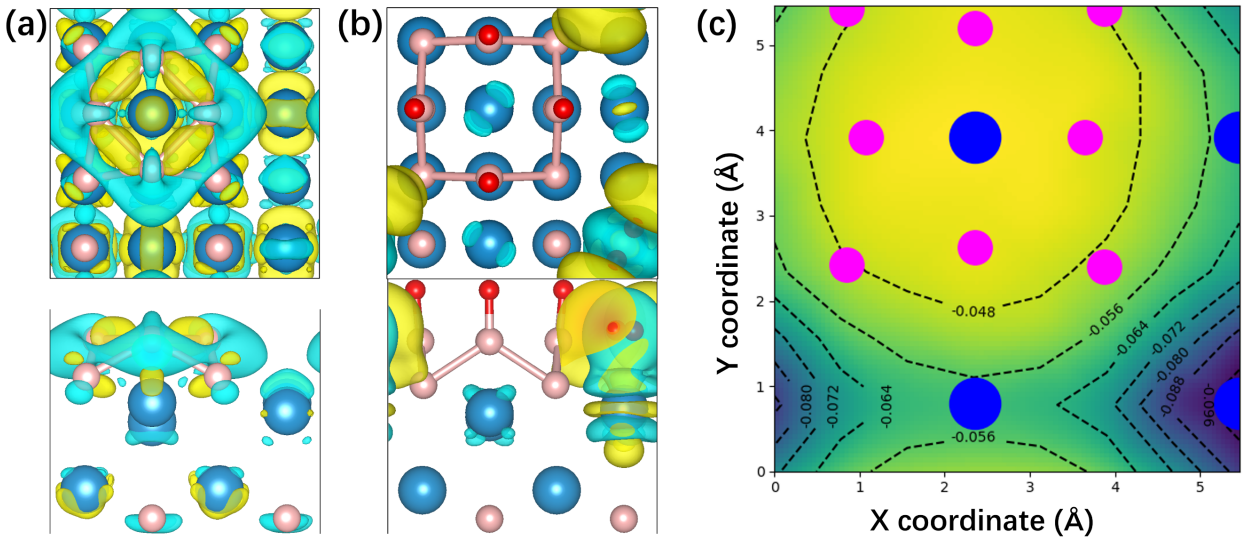

Figure 8. The electron density difference map of (a) the B_8 unit interacting with WB substrate and (b) dihydrogen-mode adsorption on type-I W in 6H global minimum configuration at isovalue=0.0015, with blue and yellow isosurfaces representing increase and decrease in electron density, respectively. (b) Potential energy surface of H_2 adsorbing on B_8-decorated surface with value-labeled contours (in eV), with warm and cold colors representing unfavorable and favorable physisorption energies, respectively. Color code: H (red), B (pink), W (blue).

CONCLUSIONS

In summary, we applied global optimization combined with DFT to explore the surface restructuring of WB (001) and the diverse adsorption configurations under different adsorbate coverage. Based on the obtained surface states from global optimization, we constructed a reaction network by checking the geometric similarity of the surface states of different coverages. A grand canonical ensemble is proposed based on the found minima to establish a phase diagram of adsorbate coverages as a function of pH and applied potential. The contribution to the overall activity by each surface state is calculated to reveal an intricated reaction network involving coexisting surface states of different adsorbate coverages and configurations. The ensemble-averaged reaction rate suggests that the HER activity heavily depends on a few states featuring the W-H/W-H_2 catalytic cycle which emerge only at higher coverages on a reconstructed surface. The population of metastable states may be further tuned by altering adsorbate coverage (solute concentration, pH), window of applied potential, temperature, controlling the over-stoichiometric amount of boron on the surface, or adding dopants to optimize the performance of the catalyst. In addition, the B_8 island is demonstrated to be H_2-phobic and could isolate the active W sites from

each other to prevent passivation of the catalysts due to H_2 bubble accumulation. Given that boron-rich interfaces are likely typical for most metal borides,[19,21] this passivation-prevention mechanism could be a general feature of HER-active borides. The study emphasizes the necessity to include surface restructuring and varying adsorbate configurations when looking for the active sites, instead of focusing on the (putative) global minimum or a static bare surface. Resorting to ensemble representation, despite the cost, has been proven rewarding given the rich chemistry it unlocked and a more realistic picture of the catalysis we can capture.

COMPUTATIONAL METHODS

The bare WB (001) is modeled by a 2x2x7 supercell with the upper three layers relaxed as surface region and lower four layers constrained as bulk region. A vacuum slab of 15 Å thickness is added in Z direction to avoid spurious interactions between periodic images.

The global optimizations for the surface terminations in B-rich conditions are performed using the particle-swarm optimization (PSO)[35] which is an efficient evolutionary algorithm for sampling of ground-state and metastable structures in complex solid or surface systems. PSO performs this sampling (search for most stable structures) by having a population of candidate geometries, which move in the search space, under the influence of their own positions and velocities, and are also guided by other geometries toward the constantly updated and currently best one. This moves the swarm toward the best solutions. The simulation is performed using the CALYPSO software,[36] following the procedure explained in a previous study.[23] The adsorbate configurations of H on B-rich surface under different coverages are exhaustively sampled by screening through all possible combinations due to relatively small chemical space. The generated structures are optimized with the RPBE functional[37] and PAW pseudopotentials[38] using the VASP program.[39–42] D3 correction

is used to account for the dispersion interactions,[43] and dipole corrections are applied to remove the artificial electrostatic fields arising from asymmetric slabs in periodic boundary conditions. The convergence criteria for geometry (SCF) was set to 10^{-5} (10^{-6}) eV and 10^{-2} eV/Å for forces. 4 x 4 x 1 Γ-centered *k*-point grid was used and the cutoff energy for the kinetic energy of the plane-waves was 450 eV. Note that although a canonical DFT scheme instead of a grand canonical DFT one is employed here, the Fermi level shift upon adding adsorbate was calculated to be ~0.05 eV, hence the results obtained should only deviate minorly from the grand canonical DFT treatments.

The surface energies were calculated as:

$$\boldsymbol{\gamma} = \frac{1}{2\boldsymbol{A}}(\boldsymbol{E}_{\text{slab}} - \sum \boldsymbol{N}_{\text{X}}\boldsymbol{\mu}_{\text{X}})$$

Where A is the area of the supercell, $\boldsymbol{E}_{\text{slab}}$ is the energy of the surface slab, $\boldsymbol{N}_{\text{X}}$ is the number of X atoms in the slab, $\boldsymbol{\mu}_{\text{X}}$ the chemical potential of the X atom. The chemical potential of W and B are calculated from bulk WB for the stoichiometric part, while from bulk FCC W and bulk elemental B for the non-stoichiometric part, respectively. The surface energy of asymmetric slabs are calculated by canceling out the contribution using a corresponding symmetric slab following the protocol explained in reference.[44]

The adsorption energy is calculated by:

$$\Delta\boldsymbol{E}_{\text{H}} = \boldsymbol{E}(* \text{H}) - \boldsymbol{E}(*) - \boldsymbol{E}(\text{H})$$

where the * stands for the adsorption site. The adsorption free energy of H is calculated by:

$$\Delta\boldsymbol{G}_{\text{H}} = \Delta\boldsymbol{E}_{\text{H}*} + \mathbf{ZPE} - \boldsymbol{T}\Delta\boldsymbol{S}_{\text{H}}$$

where the latter two terms (ZPE and entropy term at room temperature) are taken from literature

to be +0.24 eV.[27]

In the grand canonical ensemble, the population of each surface state is calculated by Boltzmann distribution based on the grand canonical free energy. The chemical potential of H^+ and e^- can be expressed using the computational hydrogen electrode model:[27]

$$\boldsymbol{\mu}_{\mathrm{H}}(U, p\mathrm{H}) = \frac{1}{2}\mu(\mathrm{H}_2) - eU + k_{\mathrm{B}}Tp\mathrm{H}$$

Where $\mu(\mathrm{H}_2)$ is the chemical potential of hydrogen molecule in gas state, and the $\boldsymbol{U}$ is referenced against the standard hydrogen electrode (SHE).

The transition states (TS) are obtained using climbing image nudged elastic band (CI-NEB) method,[45] and each TS geometry has been calculated to have only one imaginary mode. The Bader charges are calculated from VASP output using Bader Charge Analysis code.[46]

Molecular dynamics (MD) simulations are performed using VASP. The NVT ensemble simulation is performed at 500 K for 5 ps duration with time step of 1 fs. A Nose-Hoover thermostat was used, and image was collected every 50 fs after system was considered to be equilibrated.

ASSOCIATED CONTENT

Supporting Information.

The following files are available free of charge.

Surface energy of explored surface terminations, binding energy of adsorbates, geometry and relative energy of low-energy minima at 1H~8H coverages, transition states of H migration on B_8, RMSD of H-coverged B_8 during BOMD, calculated Bader charges, and a list of chemically relevant reaction pairs.

ACKNOWLEDGMENT

This work was funded by DOE-BES grant DE-SC0019152. This research used resources of the National Energy Research Scientific Computing Center (NERSC), a U.S. Department of Energy Office of Science User Facility operated under Contract No. DE-AC02-05CH11231. An award of computer time was provided by the Innovative and Novel Computational Impact on Theory and Experiment (INCITE) program. This research used resources of the Argonne Leadership Computing Facility, which is a DOE Office of Science User Facility supported under Contract DE-AC02-06CH11357.

AUTHOR INFORMATION

Corresponding Author

*Corresponding Author's email: ana@chem.ucla.edu

Present Addresses

‡Present address: Department of Chemistry, California Institute of Technology, Pasadena, CA, 91125

REFERENCES

(1) Yan, Y.; Xia, B. Y.; Zhao, B.; Wang, X. A Review on Noble-Metal-Free Bifunctional Heterogeneous Catalysts for Overall Electrochemical Water Splitting. *J. Mater. Chem. A* **2016**, *4* (45), 17587–17603. https://doi.org/10.1039/C6TA08075H.

(2) Anantharaj, S.; Ede, S. R.; Sakthikumar, K.; Karthick, K.; Mishra, S.; Kundu, S. Recent Trends and Perspectives in Electrochemical Water Splitting with an Emphasis on Sulfide, Selenide, and Phosphide Catalysts of Fe, Co, and Ni: A Review. *ACS Catal.* **2016**, *6* (12), 8069–8097. https://doi.org/10.1021/acscatal.6b02479.

(3) Carenco, S.; Portehault, D.; Boissière, C.; Mézailles, N.; Sanchez, C. Nanoscaled Metal Borides and Phosphides: Recent Developments and Perspectives. *Chem. Rev.* **2013**, *113* (10), 7981–8065. https://doi.org/10.1021/cr400020d.

(4) Alexandrova, A. N.; Boldyrev, A. I.; Zhai, H.-J.; Wang, L.-S. All-Boron Aromatic Clusters as Potential New Inorganic Ligands and Building Blocks in Chemistry. *Coord. Chem. Rev.* **2006**, *250* (21), 2811–2866. https://doi.org/https://doi.org/10.1016/j.ccr.2006.03.032.

(5) Scheifers, J. P.; Zhang, Y.; Fokwa, B. P. T. Boron: Enabling Exciting Metal-Rich Structures and Magnetic Properties. *Acc. Chem. Res.* **2017**, *50* (9), 2317–2325.

(6) Gupta, S.; Patel, N.; Miotello, A.; Kothari, D. C. Cobalt-Boride: An Efficient and Robust Electrocatalyst for Hydrogen Evolution Reaction. *J. Power Sources* **2015**, *279*, 620–625.

(7) Borodzinski, J. J.; Lasia, A. Electrocatalytic Properties of Doped Nickel Boride Based Electrodes for the Hydrogen Evolution Reaction. *J. Appl. Electrochem.* **1994**, *24* (12), 1267–1275.

(8) Jothi, P. R.; Zhang, Y.; Scheifers, J. P.; Park, H.; Fokwa, B. P. T. Molybdenum Diboride Nanoparticles as a Highly Efficient Electrocatalyst for the Hydrogen Evolution Reaction. *Sustain. Energy Fuels* **2017**, *1* (9), 1928–1934. https://doi.org/10.1039/C7SE00397H.

(9) Jothi, P. R.; Zhang, Y.; Yubuta, K.; Culver, D. B.; Conley, M.; Fokwa, B. P. T. Abundant Vanadium Diboride with Graphene-like Boron Layers for Hydrogen Evolution. *ACS Appl. Energy Mater.* **2019**, *2* (1), 176–181. https://doi.org/10.1021/acsaem.8b01615.

(10) Park, H.; Zhang, Y.; Lee, E.; Shankhari, P.; Fokwa, B. P. T. High-Current-Density HER Electrocatalysts: Graphene-like Boron Layer and Tungsten as Key Ingredients in Metal Diborides. *ChemSusChem* **2019**, *12* (16), 3726–3731. https://doi.org/10.1002/cssc.201901301.

(11) Robinson, P. J.; Liu, G.; Ciborowski, S.; Martinez-Martinez, C.; Chamorro, J. R.; Zhang, X.; McQueen, T. M.; Bowen, K. H.; Alexandrova, A. N. Mystery of Three Borides: Differential Metal–Boron Bonding Governing Superhard Structures. *Chem. Mater.* **2017**, *29* (23), 9892–9896.

(12) Li, Q.; Zhou, D.; Zheng, W.; Ma, Y.; Chen, C. Anomalous Stress Response of Ultrahard WB n Compounds. *Phys. Rev. Lett.* **2015**, *115* (18), 185502.

(13) Itoh, H.; Matsudaira, T.; Naka, S.; Hamamoto, H.; Obayashi, M. Formation Process of Tungsten Borides by Solid State Reaction between Tungsten and Amorphous Boron. *J. Mater. Sci.* **1987**, *22* (8), 2811–2815.

(14) Matsudaira, T.; Itoh, H.; Naka, S.; Hamamoto, H.; Obayashi, M. Synthesis and Reaction Sintering of WB. *Int. J. High Technol. Ceram.* **1987**, *3* (4), 337–338.

(15) Yeung, M. T.; Mohammadi, R.; Kaner, R. B. Ultraincompressible, Superhard Materials. *Annu. Rev. Mater. Res.* **2016**, *46*, 465–485.

(16) Fan, C.; Liu, C.; Peng, F.; Tan, N.; Tang, M.; Zhang, Q.; Wang, Q.; Li, F.; Wang, J.; Chen, Y. Phase Stability and Incompressibility of Tungsten Boride (WB) Researched by in-Situ High Pressure x-Ray Diffraction. *Phys. B Condens. Matter* **2017**, *521*, 6–12.

(17) Dong, H.; Dorfman, S. M.; Chen, Y.; Wang, H.; Wang, J.; Qin, J.; He, D.; Duffy, T. S. Compressibility and Strength of Nanocrystalline Tungsten Boride under Compression to 60 GPa. *J. Appl. Phys.* **2012**, *111* (12), 123514.

(18) Kayhan, M.; Hildebrandt, E.; Frotscher, M.; Senyshyn, A.; Hofmann, K.; Alff, L.; Albert, B. Neutron Diffraction and Observation of Superconductivity for Tungsten Borides, WB and W2B4. *Solid state Sci.* **2012**, *14* (11–12), 1656–1659.

(19) Grant, J. T.; McDermott, W. P.; Venegas, J. M.; Burt, S. P.; Micka, J.; Phivilay, S. P.; Carrero, C. A.; Hermans, I. Boron and Boron-Containing Catalysts for the Oxidative Dehydrogenation of Propane. *ChemCatChem* **2017**, *9* (19), 3623–3626. https://doi.org/10.1002/cctc.201701140.

(20) Grant, J. T.; Carrero, C. A.; Goeltl, F.; Venegas, J.; Mueller, P.; Burt, S. P.; Specht, S. E.; McDermott, W. P.; Chieregato, A.; Hermans, I. Selective Oxidative Dehydrogenation of Propane to Propene Using Boron Nitride Catalysts. *Science (80-.).* **2AD**, *354* (6319), 1570–1573.

(21) Zhang, Z.; Jimenez-Izal, E.; Hermans, I.; Alexandrova, A. N. Dynamic Phase Diagram of Catalytic Surface of Hexagonal Boron Nitride under Conditions of Oxidative Dehydrogenation of Propane. *J. Phys. Chem. Lett.* **2019**, *10* (1), 20–25. https://doi.org/10.1021/acs.jpclett.8b03373.

(22) Venegas, J. M.; Zhang, Z.; Agbi, T. O.; McDermott, W. P.; Alexandrova, A.; Hermans, I. Why Boron Nitride Is Such a Selective Catalyst for the Oxidative Dehydrogenation of Propane. *Angew. Chemie Int. Ed.* **2020**, *59* (38), 16527–16535. https://doi.org/10.1002/anie.202003695.

(23) Cui, Z.-H.; Jimenez-Izal, E.; Alexandrova, A. N. Prediction of Two-Dimensional Phase of Boron with Anisotropic Electric Conductivity. *J. Phys. Chem. Lett.* **2017**, *8* (6), 1224–1228.

(24) De La Pierre, M.; Bruno, M.; Manfredotti, C.; Nestola, F.; Prencipe, M.; Manfredotti, C. The (100),(111) and (110) Surfaces of Diamond: An Ab Initio B3LYP Study. *Mol. Phys.* **2014**, *112* (7), 1030–1039.

(25) Li, X.; Wang, Y. X.; Lo, V. C. First-Principles Study of the (001) and (110) Surfaces of Superhard ReB2. *Thin Solid Films* **2012**, *520* (15), 4951–4955.

(26) Silvi, B.; Savin, A. Classification of Chemical Bonds Based on Topological Analysis of Electron Localization Functions. *Nature* **1994**, *371* (6499), 683–686.

(27) Nørskov, J. K.; Bligaard, T.; Logadottir, A.; Kitchin, J. R.; Chen, J. G.; Pandelov, S.; Stimming, U. Trends in the Exchange Current for Hydrogen Evolution. *J. Electrochem. Soc.* **2005**, *152* (3), J23–J26.

(28) Lindgren, P.; Kastlunger, G.; Peterson, A. A. A Challenge to the G~ 0 Interpretation of Hydrogen Evolution. *ACS Catal.* **2019**, *10* (1), 121–128.

(29) Melander, M. M. Grand Canonical Rate Theory for Electrochemical and Electrocatalytic Systems I: General Formulation and Proton-Coupled Electron Transfer Reactions. *J. Electrochem. Soc.* **2020**, *167* (11), 116518.

(30) Bligaard, T.; Nørskov, J. K.; Dahl, S.; Matthiesen, J.; Christensen, C. H.; Sehested, J. The Brønsted–Evans–Polanyi Relation and the Volcano Curve in Heterogeneous Catalysis. *J. Catal.* **2004**, *224* (1), 206–217. https://doi.org/https://doi.org/10.1016/j.jcat.2004.02.034.

(31) Zhang, Z.; Zandkarimi, B.; Alexandrova, A. N. Ensembles of Metastable States Govern Heterogeneous Catalysis on Dynamic Interfaces. *Acc. Chem. Res.* **2020**, *53* (2), 447–458. https://doi.org/10.1021/acs.accounts.9b00531.

(32) Karmodak, N.; Andreussi, O. Catalytic Activity and Stability of Two-Dimensional Materials for the Hydrogen Evolution Reaction. *ACS Energy Lett.* **2020**, *5* (3), 885–891.

(33) Hörmann, N. G.; Andreussi, O.; Marzari, N. Grand Canonical Simulations of Electrochemical Interfaces in Implicit Solvation Models. *J. Chem. Phys.* **2019**, *150* (4), 41730.

(34) Lu, Z.; Zhu, W.; Yu, X.; Zhang, H.; Li, Y.; Sun, X.; Wang, X.; Wang, H.; Wang, J.; Luo, J.; et al. Ultrahigh Hydrogen Evolution Performance of Under-Water "Superaerophobic" MoS2 Nanostructured Electrodes. *Adv. Mater.* **2014**, *26* (17), 2683–2687. https://doi.org/10.1002/adma.201304759.

(35) Wang, Y.; Lv, J.; Zhu, L.; Ma, Y. Crystal Structure Prediction via Particle-Swarm Optimization. *Phys. Rev. B* **2010**, *82* (9), 94116.

(36) Wang, Y.; Lv, J.; Zhu, L.; Ma, Y. CALYPSO: A Method for Crystal Structure Prediction. *Comput. Phys. Commun.* **2012**, *183* (10), 2063–2070.

(37) Hammer, B.; Hansen, L. B.; Nørskov, J. K. Improved Adsorption Energetics within Density-Functional Theory Using Revised Perdew-Burke-Ernzerhof Functionals. *Phys. Rev. B* **1999**, *59* (11), 7413.

(38) Kresse, G.; Joubert, D. From Ultrasoft Pseudopotentials to the Projector Augmented-Wave Method. *Phys. Rev. b* **1999**, *59* (3), 1758.

(39) Kresse, G.; Furthmüller, J. Efficiency of Ab-Initio Total Energy Calculations for Metals and Semiconductors Using a Plane-Wave Basis Set. *Comput. Mater. Sci.* **1996**, *6* (1), 15–50.

(40) Kresse, G.; Furthmüller, J. Efficient Iterative Schemes for Ab Initio Total-Energy Calculations Using a Plane-Wave Basis Set. *Phys. Rev. B* **1996**, *54* (16), 11169–11186. https://doi.org/10.1103/PhysRevB.54.11169.

(41) Kresse, G.; Hafner, J. Ab Initio Molecular Dynamics for Liquid Metals. *Phys. Rev. B* **1993**, *47* (1), 558.

(42) Kresse, G.; Hafner, J. Ab Initio Molecular-Dynamics Simulation of the Liquid-Metal–Amorphous-Semiconductor Transition in Germanium. *Phys. Rev. B* **1994**, *49* (20), 14251.

(43) Grimme, S.; Antony, J.; Ehrlich, S.; Krieg, H. A Consistent and Accurate Ab Initio Parametrization of Density Functional Dispersion Correction (DFT-D) for the 94 Elements H-Pu. *J. Chem. Phys.* **2010**, *132* (15), 154104.

(44) Tougerti, A.; Methivier, C.; Cristol, S.; Tielens, F.; Che, M.; Carrier, X. Structure of Clean and Hydrated α-Al 2 O 3 (11 [Combining Macron] 02) Surfaces: Implication on Surface Charge. *Phys. Chem. Chem. Phys.* **2011**, *13* (14), 6531–6543.

(45) Henkelman, G.; Uberuaga, B. P.; Jónsson, H. A Climbing Image Nudged Elastic Band Method for Finding Saddle Points and Minimum Energy Paths. *J. Chem. Phys.* **2000**, *113* (22), 9901–9904. https://doi.org/10.1063/1.1329672.

(46) Yu, M.; Trinkle, D. R. Accurate and Efficient Algorithm for Bader Charge Integration. *J. Chem. Phys.* **2011**, *134* (6), 64111.

TOC graphics:

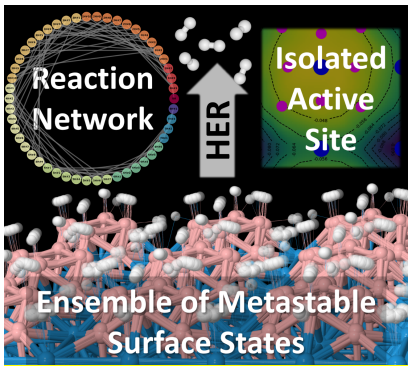

(now 5.34 cm x 4.75 cm)